IOP Publishing Semiconductor Science and Technology
Semicond. Sci. Technol. 34 (2019) 025014 (13pp) https://doi.org/10.1088/1361-6641/aaf9ed

Mg induced compositional change in InGaN alloys

Iulian Gherasoiu[1], Kin Man Yu[2,4], Michael Hawkridge[3], Lothar A Reichertz[4] and Wladek Walukiewicz[4]

[1] College of Engineering, SUNY Polytechnic Institute, Utica, New York, United States of America
[2] Department of Physics, City University of Hong Kong, Kowloon Tong, People's Republic of China
[3] PANalytical, Westborough, Massachusetts, United States of America
[4] Material Sciences Division, Lawrence Berkeley National Laboratory, Berkeley, California, United States of America

E-mail: gherasi@sunyit.edu

Received 17 October 2018, revised 11 December 2018
Accepted for publication 19 December 2018
Published 21 January 2019

Abstract

Tunnel junctions are indispensable elements of multi-junction solar cells. The fabrication of InGaN tunnel junctions requires the growth of degenerately doped n- and p-type layers. While highly doped n-type InGaN films have been demonstrated, the growth of degenerately p-doped InGaN films and the fabrication of high indium fraction InGaN tunnel junctions is still to be demonstrated. We present an investigation of the effect of Mg doping on the InGaN crystal properties over a large range of Mg fluxes and InN mole fractions in the range from 30% to 40%, using multiple characterization techniques. InGaN thin films were grown on GaN/sapphire templates and doped with Mg using plasma-assisted molecular beam epitaxy (PAMBE). We have found that the Mg concentration in the film increases linearly with the Mg beam equivalent pressure (BEP) at first, followed by a saturation at $\sim 4 \times 10^{21}\,\mathrm{cm}^{-3}$ similar to the Mg doping behavior reported for GaN. The growth rate of the alloy changes by more than 50% with the changes in the surface availability of Mg. These effects can be explained through the saturation of the atomic sites available for incorporation in the case of Mg concentration saturation and by the passivation of the free nitrogen radicals in the case of the growth rate variation. The incorporation of In and Ga depends on the flux ratio $(\Phi_{In} + \Phi_{Ga})/(\Phi_{Mg})$ at the growth surface and it is shown that the decrease of this ratio below a threshold of $\sim$2000 causes the almost complete loss of In and the formation of a new quaternary wide band gap semiconductor alloy (InGaMg)N.

Keywords: InGaN, Mg-doped P-type InGaN, plasma-assisted molecular beam epitaxy, in incorporation, tunnel junction, (InGaMg)N alloy

1. Introduction

To date there is a limited number of materials that can be used for the fabrication of cost efficient tandem solar cells. InGaN alloys have a direct band gap that is tunable across the entire solar spectrum, from 3.4 to 0.65 eV and therefore suitable for the fabrication of multiple-junction solar cells or as the top cell on a Silicon tandem structure [1]. For example, the addition of a single InGaN solar cell with a band gap of 1.8 eV on a Si cell can increase the efficiency from ~18% (Si only) to ~31% under 1 sun (AM1.5 G) standard illumination [2], while dual InGaN junctions could allow the achievement of efficiencies as high as 35% [3]. In each case the operation of the series InGaN subcells would require the formation of tunnel junctions in InGaN with indium concentrations of 69%–37% (1.15–2 eV). Despite these advantages the realization of efficient InGaN solar cells with high indium composition continues to be a formidable challenge although a great deal of work toward the understanding of the material properties has been carried out. Hence the fabrication of an efficient InGaN based multi-junction solar cell is yet to be demonstrated.

Typical tunnel junctions have p- and n-layers with a thickness of 10 –15 nm and carrier concentrations in the range

from 10^{19} to $10^{20}\,cm^{-3}$ [4, 5], ensuring that the depleted region at the interface has a width of only a few nanometers. Growing optimally doped InGaN absorber layers or tunnel junctions is still difficult due to the presence of native point defects as well as the formation of misfit dislocations and inversion domains particularly in materials with high In content. Degenerate doping of a p–n junction reduces the depletion region width while the high density of opposite charges creates an electric field that bends the bands at the junction allowing the conduction band edge to position at or below the valence band edge. In general, the layers of a tunnel junction are considered degenerately n-doped when $(E_C–E_F) \leqslant 3kT$ or degenerately p-doped $(E_F–E_V) \leqslant 3kT$ [6]. For III–V semiconductors the p- and n-side of these junctions must be doped to carrier densities in the range of low $10^{19}\,cm^{-3}$ to satisfy these conditions. For GaN at room temperature the Mott transition takes place for a carrier concentration of $\sim 1 \times 10^{19}\,cm^{-3}$ [7]. In our growth experiments, we have shown that in the case of n-type doping of GaN and InGaN with Ge it is possible to produce electron concentrations in the range from 4 to $8 \times 10^{20}\,cm^{-3}$ [8].

P-type doping of GaN and InGaN alloys is more difficult because magnesium is the only dopant that can be effectively used to obtain p-type conduction. The activation energy of the Mg acceptor was estimated at 230 meV [9] from *ab initio* calculations and experimentally found to be in the range from 124 to 212 meV depending on the Mg concentration, when used for GaN doping [10, 11]. When used for InGaN doping the activation energy of Mg acceptors decreases with the increase of indium fraction and for alloys with a fraction in the range from 2% to 35% the activation energy was found to decrease in the range from 145 meV to 43 meV, respectively [12, 13]. The dependance of the activation energy of Mg acceptor on the InGaN composition and Mg concentration has been studied and modeled recently [14]. The relatively large activation energy of Mg leads to a low acceptor ionization efficiency and usually results in low hole concentrations $(10^{17}–10^{18}\,cm^{-3})$ at room temperature. Furthermore, the measurement of the hole concentrations becomes difficult for indium fractions $\geqslant$35% as the conduction band edge of InGaN descends below the Fermi stabilization energy level (E_{FS}) and the conduction electrons form an accumulation layer at the surface [15]. In this case the bulk net acceptor concentration can only be measured with techniques such as electrochemical capacitance-voltage (ECV) which can probe the charge density below this electron accumulation layer.

In this paper, we present the investigation of the effect of Mg doping on the InGaN crystal properties over a large range of Mg fluxes and indium fractions in the range from 30% to 40%, using secondary ion mass spectroscopy (SIMS), Rutherford back scattering spectroscopy (RBS), atomic force microscopy (AFM), electrochemical capacitance-voltage (ECV), x-ray diffraction (XRD) and transmission electron microscopy (TEM).

We have found that the doping efficiency of Mg in GaN is limited due the formation of compensating defects [8], while that in InGaN is limited due the thermodynamic processes leading to the depletion of indium from the surface. We propose a model explaining this phenomenon that is supported by the experimental observations. We demonstrate a growth method that avoids indium depletion and allows the doping of the material at degenerate levels.

Finally, the effectiveness of the doping was verified through the fabrication of InGaN pn-junctions that have demonstrated electroluminescence with a central wavelength of 596 nm (~2.1 eV).

2. Experimental

InGaN thin films were grown on 5 μm thick GaN-on-sapphire templates and doped with Mg at effusion cell temperatures between 300 °C and 390 °C using a production style molecular beam epitaxy (MBE) system (GEN 200) equipped with two radio-frequency plasma sources and effusion cells for Al, Ga, In, Ge and Mg. The epitaxial growth of InGaN takes place at a temperature of 565 °C as determined using an IR pyrometer, with indium and gallium impinging fluxes of 5.5×10^{-7} Torr and 1.0×10^{-7} Torr, respectively. The total nitrogen flow (both sources) was constant at 6.4 sccm with an input power of 400 W for each plasma source. The flux beam equivalent pressure was measured before each growth run using the Bayard-Alpert pressure gauge of the beam monitor. We have chosen to use BEP to represent the Mg flux at the surface instead of an alternate measure, monolayers s^{-1}. The latter is calculated using the growth rate of the film and thus represents the material that was incorporated, disregarding the surface re-evaporation that is significant in the case of Mg. During the growth, an open-loop metal modulated epitaxy (MME) technique was used to switch the growth conditions at the surface between nitrogen-rich and metal-rich [16, 17]. Continuous monitoring of the surface using reflection high energy electron diffraction (RHEED) equipment to determine the metal coverage of the surface allows the metal shutter opening or closing based on the intensity of the RHEED pattern while the nitrogen plasma shutters are open continuously. This method enables the autonomous operation of the Ga and In effusion cell shutters avoiding the metal accumulation. However, uninterrupted exposure of the RHEED screen to desorbed fluxes produces a gradual diminution of the RHEED intensity due the re-deposition of the evaporated material on the RHEED screen, making the continuous, long-term monitoring impractical. A workaround the problem is the calibration of the effusion cells shutter On/Off instances using the RHEED monitoring in a test run before the actual sample growth, followed by the open-loop operation of the system. Typical Ga shutter ratio for GaN growth was 50 s/10 s and for InGaN growth Ga and In shutter ratio was of 46 s/14 s. With no RHEED real-time feedback however, growth conditions have often drifted to metal-rich toward the end of growth.

The surface morphology was evaluated using a Dimensions 3100 atomic force microscopy (AFM). Mg incorporation was verified, and composition and the thickness of the films were evaluated by Rutherford back scattering spectrometry (RBS) and secondary ion mass spectrometry (SIMS),

Table 1. Mg effusion cell data and characterization data for the set of samples A0–A4 and B1–B3.

Sample ID	T_{Mg} (°C)	Mg BEP (Torr)	Mg SIMS (cm^{-3})	Film thickness (nm)	Composition (%)			Acceptors ECV (cm^{-3})
					In	Mg	Ga	
A0	n.a	n.a.	n.a.	248	32	0	68	n-type
A1	390	1.62×10^{-7}	4×10^{21}	186	0.1	9.1	90.8	n-type
A2	380	1.05×10^{-7}	4×10^{21}	166	0.2	9.1	90.7	insulating
A3	370	6.8×10^{-8}	4×10^{21}	194	0.3	9.1	90.6	insulating
A4	320	7.8×10^{-9}	3×10^{21}	180	4.6	7.0	88.4	n and p-type
B1	335	4.97×10^{-9}	3×10^{21}	296	29.7	7.7	62.6	n and p-type
B2	320	2.6510^{-9}	1.4×10^{21}	330	32.4	3.6	64.0	p-type
B3	300	1.0910^{-9}	6.0×10^{20}	264	38.7	1.6	59.7	p-type

while crystallinity of the films was evaluated using the ion channeling and x-ray diffraction (XRD). Bright field mode transmission electron microscope (TEM) images were recorded for the analysis of the structural defects induced through the high incorporation of Mg in the InGaN.

3. Results and discussion

The growth starts with the addition of 100 nm of GaN over the template, followed by the opening of the indium and magnesium shutters allowing In and Mg to reach the growth surface. The first sample (A0) was grown as a reference for the InGaN properties while the rest of the A samples were grown using a continuous magnesium flux and with a decreasing magnesium cell temperature, as indicated in table 1. For the sample series B, the Mg flux was controlled through lowering the cell temperature and through the On/Off shuttering the Mg effusion cell with a ratio of 1/3. As a consequence, an effective BEP equivalent flux was calculated considering this ratio. Mg concentrations in the samples were estimated from SIMS spectra at a depth of 50 nm. Similarly, the composition of the samples (In, Ga, Mg) was determined from the SIMS data while RBS measurements were used to confirm or determine the compositional depth profile for the elements with a high atomic number, Ga and In.

During the growth of these samples the substrate temperature, indium and gallium fluxes were kept constant for all the samples analyzed.

3.1. Liquid phase epitaxy

It is widely accepted that the presence of excess metal on the surface is beneficial for the surface diffusion of the precursors, and it was found that GaN films grown by PAMBE within Ga-droplet regime exhibit complete surface coverage of metallic Ga and provides subsequently the highest N^*adatom mobility [18]. Similarly, it was found that during the growth of InGaN on (0001) surfaces, 1–2 monolayers of indium provide increased diffusivity for the nitrogen radicals (N^*) in between the metal layers, preventing their accumulation [19]. Following along the idea of excess Ga on the growth surface, it was proposed that active nitrogen supersaturates the layer of metallic Ga, leading to the formation of GaN at the interface between the solid GaN and the liquid Ga. According to this model the growth takes place under liquid phase epitaxy (LPE) conditions [20].

We bring further evidence that LPE is the process that takes place at the surface of the GaN and InGaN films that are grown under metal-rich conditions. For this purpose, the re-evaporation of Ga and In during the PAMBE of GaN/InGaN structure was monitored during the growth of the sample A0, using a residual gas analyzer (RGA) system pointing toward the growth surface. The readings of the RGA during the growth are further correlated with the sample structure as determined by RBS measurements. The RGA operating in 'Pressure versus time' mode records the partial pressures for selectd masses, in this case Ga and In, providing a time history of the desorption from the surface of the two elements. Depictions along vertical columns in figures 1(a)–(c) represent the elemental model measured using RBS – left side column, a suggesive atom model of growth evolution—central column and the partial pressure versus time recording—right side column, corresponding to the material desorption stages identified in the RGA measurements. The spurious peaks visible ocasionally during the recording are artefacts of the RGA operation generated when previously adsobed gases desorb on the hot filament producing momentary streams of ions. Their frequecy decreases as the growth proceeds.

During the first stage, GaN is grown and only N-plasma and Ga-1 cell (Φ_{Ga1}) shutters are open. As can be seen in figure 1(a), Ga is incorporated efficiently, as demonstrated by the negligible desorption flux (red trace: $\sim 1.2 \times 10^{-12}$ Torr), suggesting that sufficient nitrogen is available at the growth interface. The active nitrogen diffuses through a wetting layer of Ga before incorporation at the solid interface. During this time, a thin GaN layer is formed on top of the GaN template as determined by RBS.

Figure 1(b) represents the moment in which the indium shutter is opened, and indium reaches the growth surface. At the same time Ga flux is decreased by switching the flux to a lower temperature cell, Ga-2, with a flux $\Phi_{Ga2} < \Phi_{Ga1}$. It is noticeable that the Ga desorption remains steady, almost unchanged (red trace: $\sim 1.2 \times 10^{-12}$ Torr), while In desorption from the surface is about one order of magnitude larger, Φ_{In1}, suggesting that there is excess In that cannot form

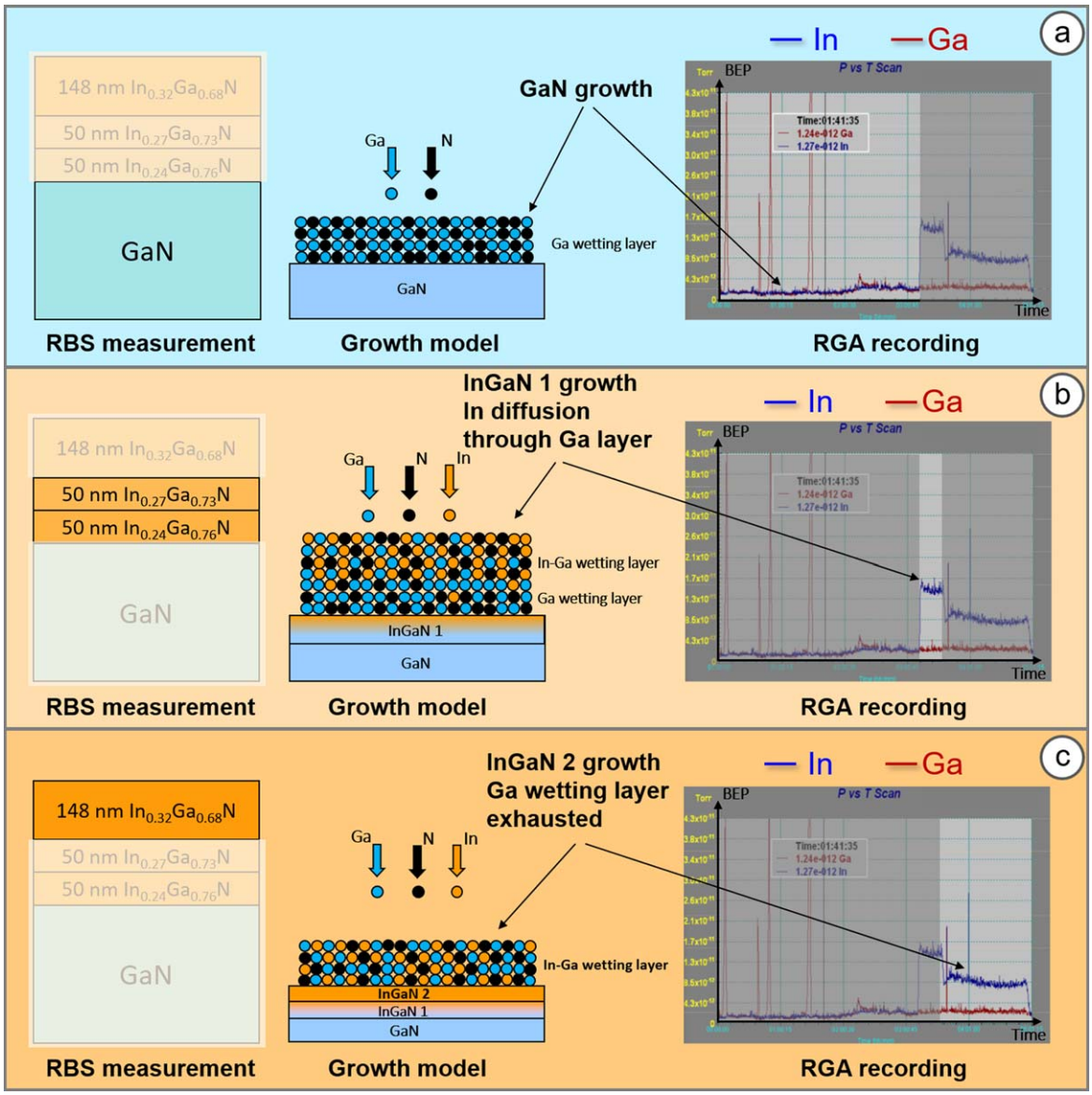

Figure 1. RGA signal during the growth transition from GaN to InGaN. The measurement demonstrates the presence of a Ga wetting layer covering the growth surface that is exhausted as the growth proceeds. (a) Ga desorption during the growth of GaN film; In signal is just the instrument background since no In is desorbing; (b) Ga, In desorption after the opening of the In shutter during the initiating of the InGaN growth; (c) Ga, In desorption during InGaN growth, after the Ga wetting layer is exhausted through incorporation in the film.

stable bonds with N and cannot reach the growth surface to incorporate. As a result, this excess is eventually re-evaporated. For this growth stage, RBS finds that an InGaN transition layer starts to form at the surface, with the In fraction changing from 24% to 27%. The In desorption drops sharply to Φ_{In2} after ~10 min of growth. The In desorption flux behavior, together with the RBS determined transition layer, suggest that during this growth period N as well as In have to diffuse through the Ga wetting layer before reaching the solid interface. The increase of the In fraction during the growth of the transition layer suggests that the as Ga wetting layer is becoming thinner as the time progresses. The sudden decrease of the In desorption at the end of the period is associated, in this model, with the exhaustion of the Ga wetting layer that eliminates the need for In and N to diffuse and allows higher incorporation rates, as suggested by the onset of the lower In desorption.

Figure 1(c) depicts the steady In desorption, after the exhaustionof the Ga wetting layer, during the growth of constant InGaN composition with an In fraction of 32%. The wetting layer in this stage of the growth is formed by a mixture of Ga and In atoms through which active nitrogen still has to diffuse to reach the solid interface and contribute to the formation of the InGaN film.

The growth of InGaN starts with the opening of the In shutter (BEP 5.5 $\times$ 10^{-07} Torr) while switching the Ga flux to a lower value of 1.0 $\times$ 10^{-07} Torr from 2.4 $\times$ 10^{-07}. This growth continues until a film of approximately 50 nm is deposited. Mg cell is then opened and the growth of InGaN continues for approximately another 120 nm. The wetting

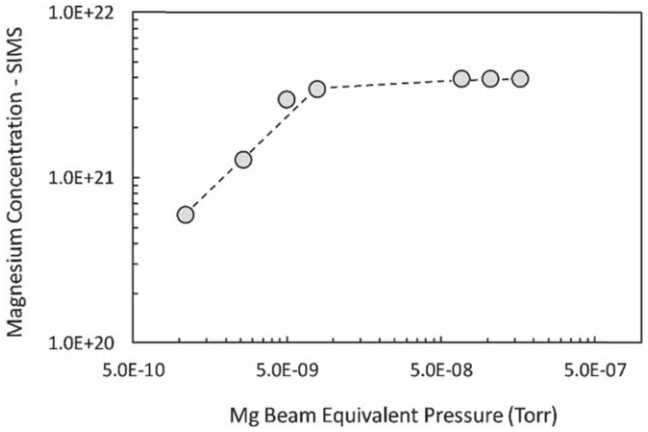

Figure 2. Mg concentrations in InGaN films measured by SIMS as a function of BEP (dashed line is just a guide for the eye).

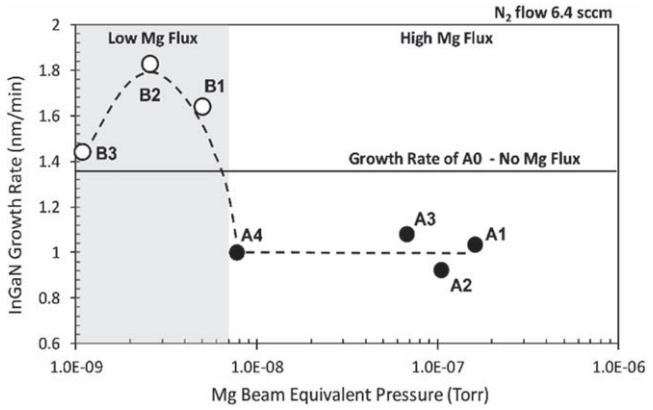

Figure 3. Growth rates of the nitride alloys as a function of the Mg flux. The continuous line represents the alloy growth rate with no Mg flux. Open circles represent the growth rate of samples for which the Mg flux was modulated while the filled circles correspond to the growth rates of the samples exposed to continuous Mg flux (dashed line is just a guide for the eye).

layer of gallium, present during the GaN growth is supplemented by indium during the growth of u-InGaN.

3.2. Continginuous Mg flux dop

The incorporation of Mg dopant in GaN has been studied previously, and it was found that after a regime in which the concentration increases linearly with the increase of the Mg flux [21], a saturation plateau is reached for which the Mg concentration levels off despite the further increase of the flux [22]. The possible mechanism responsible for Mg incorporation assumes that the surface of GaN is saturated with a layer of weakly physiosorbed Mg atoms coupled to a population of Mg chemisorbed at specific atomic sites—Ga vacancies. In this model, the incorporation of Mg is dependent on the concentration (S) of suitable surface sites. If the Mg flux Φ_{Mg} is larger than the concentration of sites S, then there will be a Mg atom available for incorporation when a site is created [21]. This mechanism is supported by *ab initio* modeling, that found that a surface phase consisting of a ¼ monolayer of Mg_{Ga} has the lowest energy for Mg adsorption. Once this surface coverage is reached the incorporation of Mg becomes independent of Mg overpressure (excess) [23]. For the case of Mg-doped InGaN we find a similar incorporation behavior. Figure 2 illustrates the relationship between the concentration of Mg in InGaN samples and the BEP. It can be observed that for Mg effective fluxes from $\sim 1 \times 10^{-9}$ Torr to $\sim 8 \times 10^{-9}$ Torr, Mg concentration increases linearly, while above this threshold, although the flux of Mg increases more than one order of magnitude, the concentration remains fixed around $4 \times 10^{21}\,cm^{-3}$.

The growth rate (GR) of nitride semiconductors has also been found to be dependent on the Mg flux. The change in surface kinetics associated with the presence of Mg has been described before in relation to Mg-doped GaN grown by PAMBE [24]. The authors found that the GR is increased by a maximum of ~35% which is similar to the increase found in the current study. However, in this study the range of Mg flux has been limited to a domain for which the decrease of the growth rate with the increase of Mg surface density was not observed. According to this study, the increase of the GR with the increase of the Mg availability is related to the formation of MgN radicals that prevent active N from recombining to form N_2 and desorb. The increased residence time of Mg passivated N allows more time for the incorporation to take place and as a result the GR increases. The maximum of the GR is reached when the Mg on the surface binds to the maximum number of N radicals that would otherwise recombine and desorb.

In our experiments the growth rate was found also to depend on the Mg flux reaching the surface. Without Mg, the growth rate of InGaN was $\sim 1.4\,nm\,min^{-1}$. The presence of a large amount of Mg on the surface leads to an accentuate decrease of the growth rate, to about $1\,nm\,min^{-1}$ or $75\% \pm 3\%$ of the un-doped GR as depicted in figure 3. Conversely, under small Mg density on the surface, an increase of the growth rate is noticeable. The increase of the GR reaches a maximum of approximately 33% followed by a decrease of the GR to the un-doped level, as Mg amount trends toward low values. We conjecture that further increase of the Mg density on the surface not only prevents the N_2 desorption, as described in [24], but since an increasing number of N radicals are tied as MgN, the formation of the epitaxial layer is delayed, leading to the decrease of the growth rate to levels below that of the undoped films, as seen in figure 3. The average Mg surface density (CS_{Mg}) can be estimated assuming a uniform Mg distribution throughout the unit volume, where CV_{Mg} is defined as the volume density measured by SIMS. Thus $CS_{Mg} = CV_{Mg}(SIMS)/n_{ML[0001]} = 4 \times 10^{21}/3.86 \times 10^{7}$, where $n_{ML[0001]}$ is the number of monolayers. Thus, the growth rate for the samples A1–A4 levels off as the Mg surface density becomes almost constant at about $1 \times 10^{14}\,atoms\,cm^{-2}$. This density is just one order of magnitude lower than that for GaN, atom surface density, $1.135 \times 10^{15}\,atoms\,cm^{-2}$ [23] and the SIMS measurements of samples A1–A4 that find a Mg concentration of around 9% correlate with it. The excess of Mg added to the surface with the increase of the flux, that does not incorporate, will likely

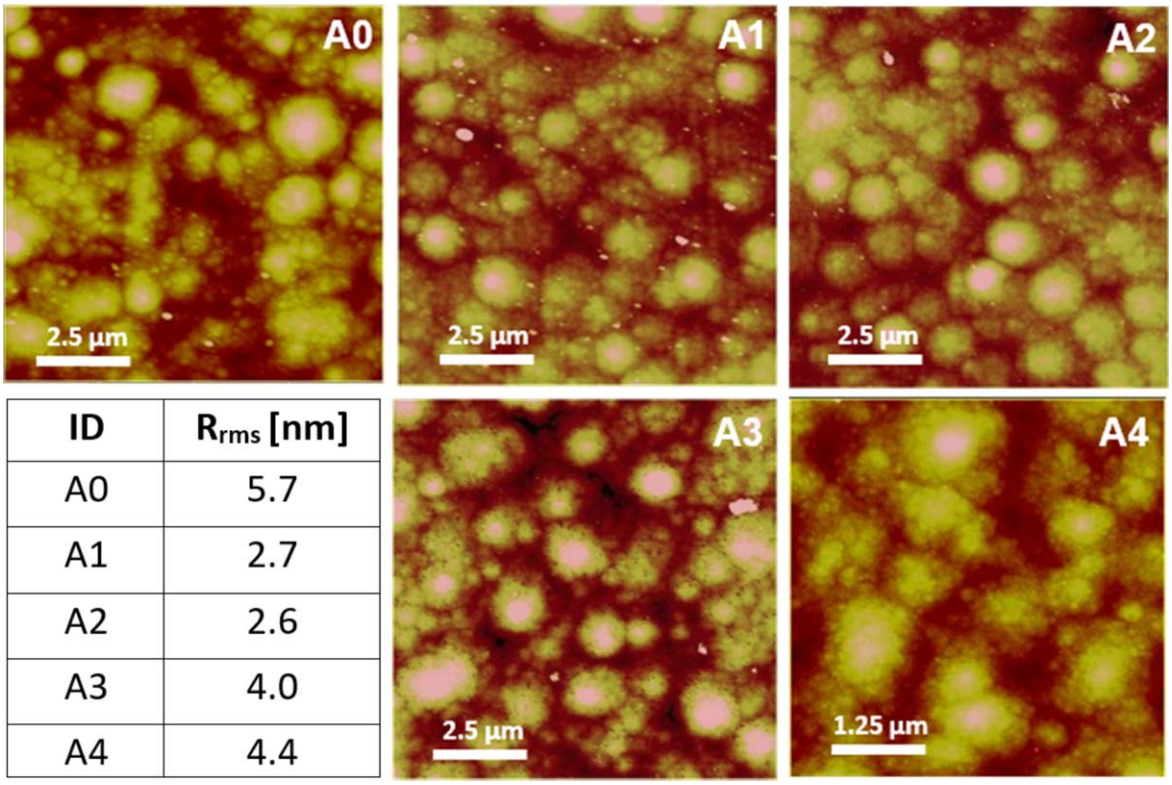

ID	R_{rms} [nm]
A0	5.7
A1	2.7
A2	2.6
A3	4.0
A4	4.4

Figure 4. AFM images of the un-doped InGaN (A0), and Mg-doped InGaN (A1, A2, A3, A4). Scans A-A3 are of ($10 \times 10\ \mu m^2$) size and A4 is of ($5 \times 5\ \mu m^2$) size.

re-evaporate or will be accumulated together with In as droplets that nucleate and develop on the surface.

Figure 4 illustrates the changes in the surface morphology that are associated with Mg doping as determined by AFM. The un-doped sample (A0) has a root-mean-squared (rms) roughness of 5.7 nm. It is noticeable that the addition of Mg reduces the surface roughness (A1, A2) to levels that are similar to those of un-doped InGaN films of the same thickness [25] and the reduction of surface Mg allows the roughness to trend back to larger values (A3, A4). This evolution supports the model in which surface Mg passivatesthe free nitrogen radicals increasing their surface diffusion range and thus producing a smoother morphology.

SIMS profiles of the samples A1–A4 reveal an unusual behavior of the In in the presence of Mg. In figure 5 it can be seen that when Mg is admitted to the growth surface, indium incorporation is drastically reduced by more than two orders of magnitude at the onset of the p-InGaN layer growth and then recovers to some extent toward the end of the growth while Ga concentration appears unaffected. The reduction of the flux of Mg with the decrease of the cell temperature (table 1) decreases the impact on In incorporation as can be seen from the evolution of indium concentration in the samples A1–A4.

The large Mg concentration ($\sim 7 \times 10^{20}\,cm^{-3}$) that appears in the film before the Mg shutter opening is attributed to the high volatility of Mg and the presence of parasitic deposits in the vicinity of the Mg crucible opening that are not screened by the cell shutter despite the use of a special double-blade shutter.

The evolution of this concentration correlates closely with the evolution of Mg cell temperature in the period prior to the shutter opening. It suggests that, for Mg doping, the use of a valved cell should be considered for a better control of the flux rather than the typical effusion cell. According to the Mg concentration in the initial 50 nm of InGaN, it can be estimated that the parasitic flux was no larger than 1×10^{-9} Torr and therefore it did not interfere with the incorporation of In.

The formation of the bulk film is strongly dependent on processes that take place at the surface and in the first few bilayers of the growing film. The lattice relaxation associated with misfit dislocations at the GaN-InGaN interface, the growth of films beyond the critical thickness and the temperature at which the growth takes place positions the InGaN analyzed in this work in the spinodal decomposition region from the onset of the growth [26].

In segregation and alloy ordering leading to compositional variation has been observed previously [27], and the predominant presence of In at the film surface can be argued based mainly on chemical effects, i.e. weaker In-N bonds as compared with Ga-N. Recently it was shown that In segregation occurs also during the coherent growth on Ga-polar surfaces [28]. In this case ([28]), a strong driving force for In segregation at the top and for In_{Ga} atoms to occupy the first surface layer was found.

Thus, when Mg doping begins, the first InGaN bilayers are expected to be predominantly occupied by In with Ga occupancy increasing in the layers beneath. It has been argued that Mg incorporation in the surface bilayer is to be expected,

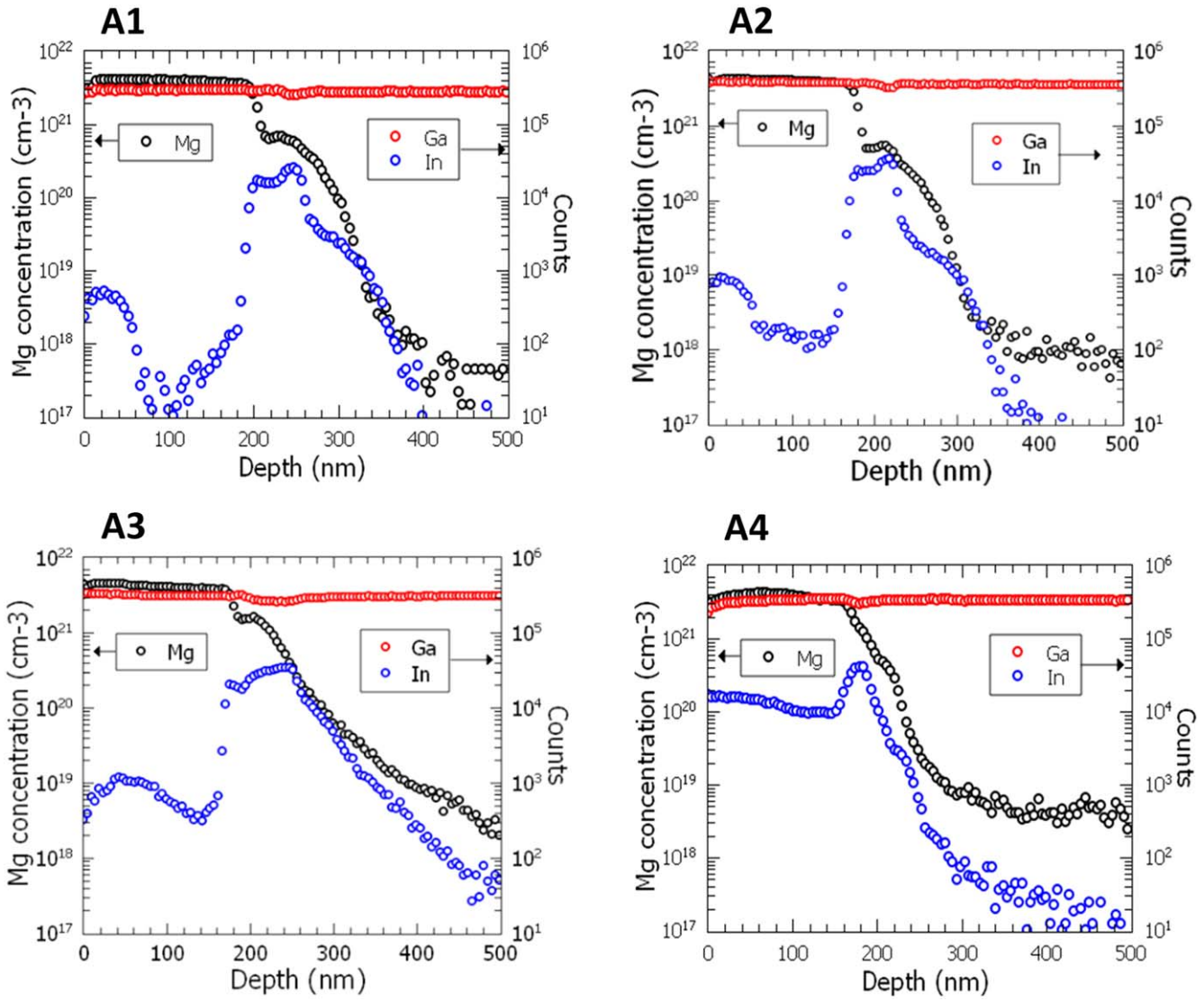

Figure 5. Mg concentration and In, Ga profiles of the InGaN:Mg films A1–A4 determined by SIMS.

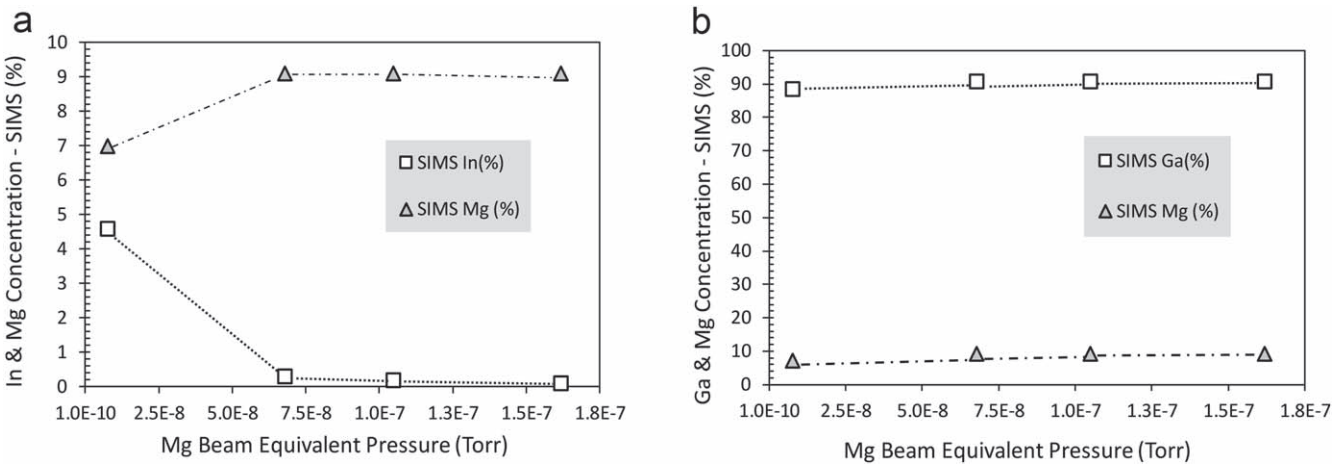

Figure 6. (a) In, and Mg fractions measured by SIMS and RBS are plotted as a function of Mg flux and (b) Ga, and Mg fractions measured by SIMS and RBS are plotted as a function of Mg flux (dashed line is just a guide for the eye).

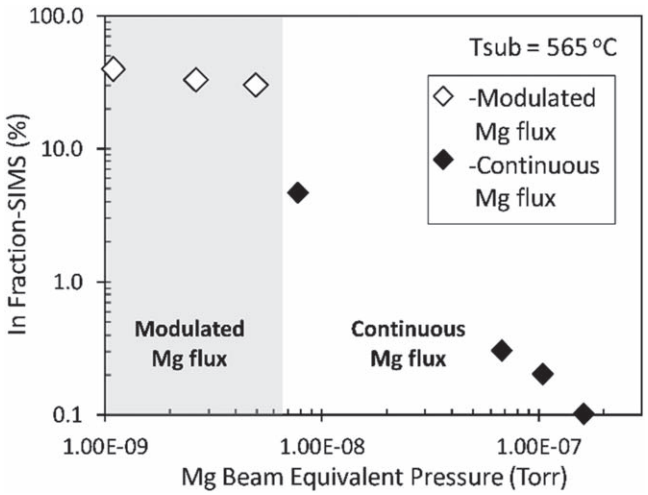

Figure 7. Indium fraction as a function of BEP and the correlation between In fraction and Mg concentration determined by SIMS.

as the substitutional Mg reduces the number of excess electrons in the clean In or Ga-terminated surfaces (MBE, hydrogen free environment) [29]. On Ga-polar surfaces, interstitial Mg or Mg on N site can displace spontaneously a Ga atom in the first layer of GaN and substitute Ga in the lattice (Mg_{Ga}) [23]. The ejected Ga becomes a part of the wetting layer and diffuses to another site. It was found that the most stable position of Mg_{Ga} is in the 3rd bilayer beneath the surface and has a formation energy higher by 0.48 eV than that in the surface layer. This demonstrates that the ability of Mg to displace Ga out of the lattice throughout the first few bilayers of GaN through a repeated kick-out mechanism decreases as Ga moves toward the bulk of the film. Similarly, Mg incorporates in the first bilayer of InN by replacing in the lattice [29]. Again, through a repeated kick-out mechanism

Mg diffuses downwards and finds the most stable position in the 3rd bilayer beneath the surface that has a formation energy higher by ∼0.9 eV when compared with that in the first bilayer. Overall, the jump of Mg toward the deeper sites requires more energy and thus is less frequent. However, once it has happened, Mg position is more stable than in shallower sites, as the energy barrier for a jump back is arguably higher —a jump back would be against the concentration gradient. The smaller size of the Mg atoms changes the bond lengths around the substitutional Mg and it is shown that in the third bilayer Mg-N distance becomes the same with that of In-N bond length (2.16 Å). The elimination of the strain in this position ensures the stability of the substitutional Mg in the lattice as it transitions toward deeper, bulk-like film, as the growth proceeds.

The picture that emerges is that of Mg diffusing through the wetting layer to the first bilayer of InGaN, that has a higher In fraction than Ga. Here Mg substitutes to In preferentially rather than to Ga as the density of In sites is larger in the first bilayer. Incoming Ga atoms are also exchanging places with In and form more stable Ga–N bonds. The roughness and the morphology of these films suggests that the growth develops in a block-flow mode (step bunching). In addition, edges of the 2nd and 3rd bilayer are available for Mg incorporation, as well. Mg can replace thus In and to a lesser extent Ga in these bilayers. As Mg becomes part of the lower bilayers it finds the most stable position starting with the 3rd bilayer [23, 29]. Since, the combined density of Ga and Mg atoms is comparable to the density of surface sites, Ga and Mg are expected to replace most of the In atoms in the first bilayer and the subsequent bilayers, thus effectively preventing the incorporation of In in the growing film. The material resulted is InGaMgN with In fractions around 1%.

For theses alloys the Mg fraction was found to be around 9% while the fraction of Ga was found to be around 91%. Figure 6 shows the concentrations of In, Ga and Mg as a function of the Mg flux. The graphs convey information related to surface processes as well as interplay processes that take place in the first few bilayers, leading to the incorporation of these elements. The influence of the surface Mg on the incorporation of In, Ga and Mg can be quantified by the correlation coefficient r of two data samples x and y of size n that is given by relationship (1), [30]:

$$r = \frac{\sum_{i-1}^{n}(x_i - \bar{x})(y_i - \bar{y})}{\sqrt{\sum_{i-1}^{n}(x_i - \bar{x})^2}\sqrt{\sum_{i-1}^{n}(y_i - \bar{y})^2}}. \quad (1)$$

We find that the In fraction (y) decreases almost linearly with the increase in the Mg flux (x), figure 6(a), trend supported also by a large, negative correlation coefficient: −0.82. One might expect that this correlation will be preserved during the processes leading to the transition in the bulk and, when the correlation between the fraction of Mg and the fraction of In incorporated, as measured by SIMS, is analyzed a large, negative coefficient of −0.99 is found. The large value of r in this case, is noticeable also from the oposite trend between Mg data and the data of In in figure 6(a). The strong correlation between surface Mg and In atoms incorporated suggests that In rejection and substitution by Mg is dominated by process at surface. The correlation between Mg and In appears even stronger in the bulk when the SIMS fractions are considered suggesting that Mg-In interaction has the significant role in establishing the amount of Mg that will eventually incorporate.

In contrast, the positive slope of the linear fit to the Ga fraction data in figure 6(b), reflected by a correlation coefficient of 0.84, indicates that Ga fraction increases with the increase of the Mg flux.

The trend suggests that the rejection of In from incorporation, mediated by surface Mg, promotes the incorporation of Ga. The coefficient of correlation between Mg fraction data and Ga fraction incorporated is 0.99. The large, positive value of the coefficient indicates that the fraction of Ga that is incorporated is strongly related to the fraction of Mg that incorporates and that more Mg in the film promotes the incorporation of Ga. These findings support the model in which Mg substitutes with predilection for In sites at the surface and in the bulk.

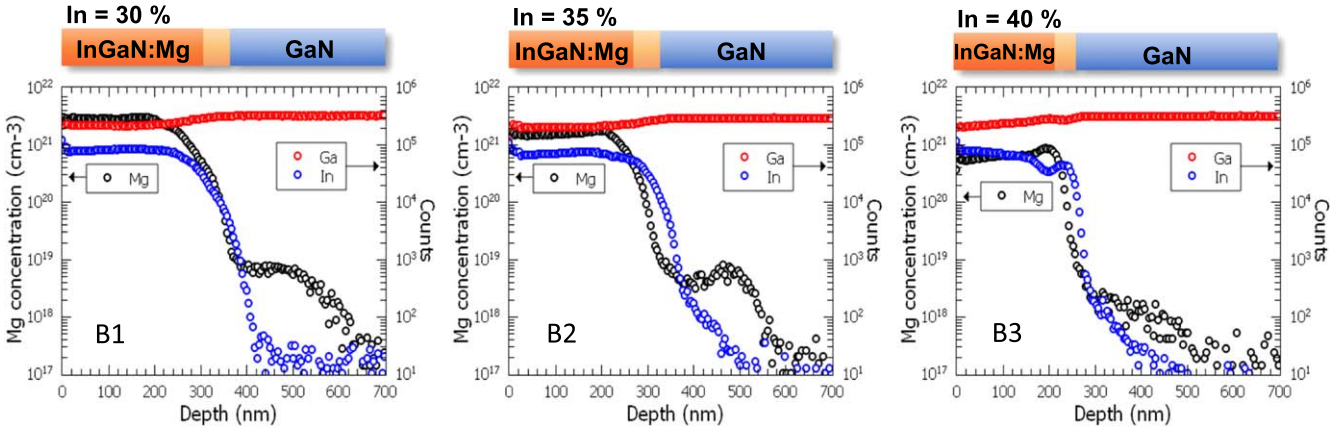

Figure 8. Mg concentration and In, Ga profiles of the InGaN:Mg films B1–B3 determined by SIMS. These samples were grown using a flux modulated doping method.

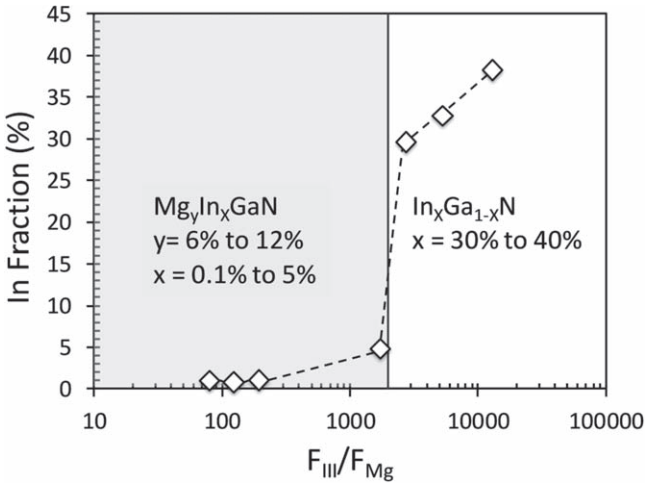

Figure 9. Indium fraction as a function of Flux ratios (F_{III}/F_{Mg}) (dashed line is just a guide for the eye).

3.3. Modulated Mg flux doping

To promote In incorporation at the surface, while also maintaining Mg incorporation, a flux modulation technique has been adopted in which the Mg flux as well as In were shuttered during the growth while the flux of the Nitrogen was admitted continuously. The Mg cell shutter On/Off ratio was 15 s/45 s. This method allows the control of the doping average flux without changing the temperature of the effusion cell as can be seen in table 1, samples B. Figure 7 also shows how the In fraction, measured by SIMS, changes with Mg BEP. Indium fraction is significantly lower than the fraction of the un-doped sample (32%) when the flux of Mg is larger than 1×10^{-8} Torr and appears not to be impacted by fluxes lower than 5×10^{-9} Torr.

Using this method, the incorporation of In was unaffected while maintaining high Mg concentrations as measured by SIMS and depicted in figure 8.

The SIMS profiles for samples grown with the Mg cell shuttering technique show uniform In concentrations throughout the InGaN film, as well as uniform Mg incorporation, despite the flux interruption, suggesting that Mg forms a constant supply source at the surface, probably through mixing with In and Ga in the wetting layer. The effect of Mg doping on the In incorporation in InGaN is further studied by considering the flux ratio of the different species during growth. The flux ratio between group III elements ($\Phi_{In} + \Phi_{Ga}$) and the flux of Φ_{Mg} was determined using measurements of the flux with the beam pressure monitor, for the range of fluxes used for the growth of the samples in table 1. The flux ratio between group III elements ($\Phi_{In} + \Phi_{Ga}$) and the flux of Φ_{Mg} was determined using measurements of the flux with the beam pressure monitor, for the range of fluxes used for the growth of the samples in table 1. The relative flux of two species can be calculated provided that corrections for relative velocities and ionization efficiencies are included according to equation (2), [30]:

$$\frac{\Phi_x}{\Phi_y} = \frac{P_x \eta_y}{P_y \eta_x} \sqrt{\frac{T_x M_y}{T_y M_x}}, \tag{2}$$

where the subscripts x and y correspond to species x and y, respectively, Φ_x is the flux of specie x, P_x is the beam equivalent pressure, T_x is the absolute temperature and M_x is the molecular weight. The ionization efficiency η_x relative to nitrogen is given by equation (3):

$$\frac{\eta_x}{\eta_N} = [(0.4Z/14) + 0.6], \tag{3}$$

where Z is the atomic number, [31].

Figure 9 shows the dependence of the measured In fraction in the InGaN layer on the group III to Mg flux ratio $(\Phi_{In} + \Phi_{Ga})/\Phi_{Mg}$. It can be observed that In incorporation is affected to a lesser degree for a flux ratio that is larger than 2000. For lower flux ratios Mg is incorporated preferentially in the place of In and the composition transitions abruptly to (InGaMg)N alloys.

3.4. TEM analysis

TEM was carried out for a detailed measurement of the crystallinity and microstructure of the InGaN samples. Figure 10 shows cross sectional TEM micrographs of samples

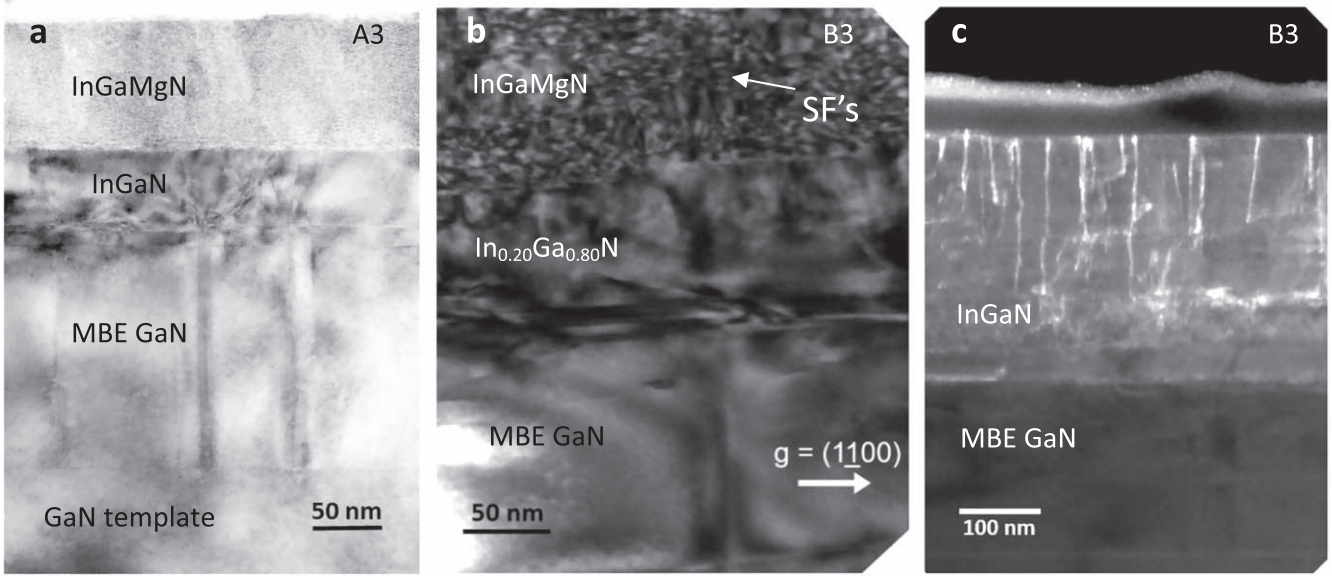

Figure 10. (a) TEM image of the cross-section of the sample A3, (b) bright-field image of the cross-section of the sample B3, (c) dark-field image of sample B3.

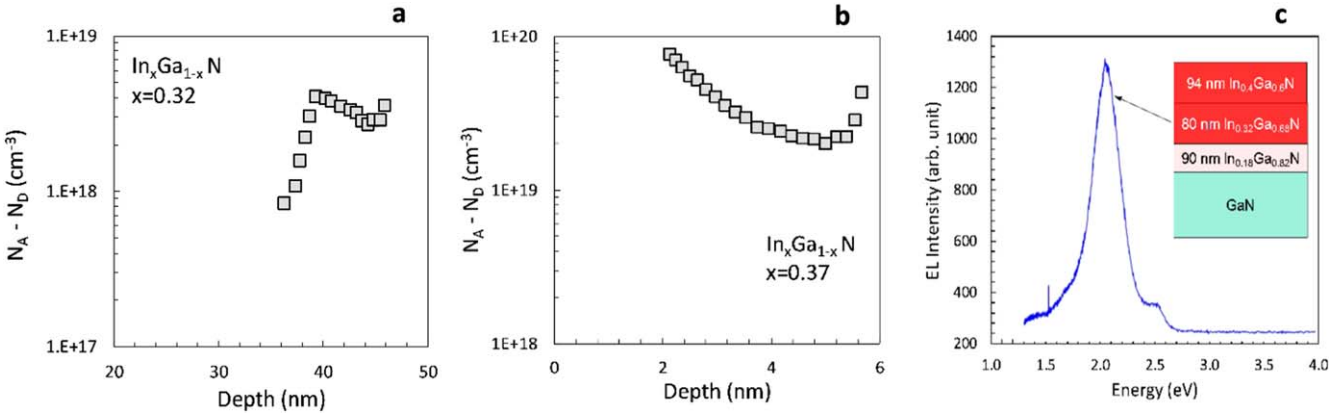

Figure 11. (a) ECV measurement of sample B2, (b) ECV of an optimized InGaN:Mg film and (c) Sample B3 - room temperature electroluminescence of the InGaN homojunction.

A3 as well as the bright-field and dark-field images of sample B3.

The nitride layers and the interface between them are clearly distinguished in the TEM image of sample A3. The defect density increases at the interface of the InGaN due the lattice mismatch to the GaN layer. A well-defined diffraction pattern (not shown) from the top (InGaMg)N layer, indicates that this layer has good crystalline quality. However, small arcs on either side of the main diffraction spots strongly oriented along the [0001] direction are also observed, and these arcs indicate a periodic structure related to compositional modulation with a period of ∼21 Å. For sample B3, similar to previous reports [32], two different layers of InGaN are apparent: a lower layer with an average In fraction of 20% that is relatively defect free, followed by a distinct interface and a higher composition InGaN (20% to 40%) that is populated by a high density of stacking faults that are visible in the bright-field image of figure 10(b). It was shown previously that stacking faults are a result of Mg doping [33] and their presence defines the upper part of InGaN of this sample that was doped with Mg. The dark-field image of this sample in figure 10(c), shows that the lower InGaN layer is relatively free of defects, while the image shows strong contrast from dislocations with a screw component that originate mostly in the Mg doped InGaN layer. Although there is no commonly accepted sequence and mechanism to explain their formation, the presence of both types of dislocations is a common feature of the lattice missmatched InGaN/GaN heterostructures [34].

3.5. Electrical characterization

Conduction type and carrier concentration were measured using ECV. Sample B1 has shown an unstable conduction type which was dependent on the location of the measurement, suggesting that the density of the acceptors is roughly equal to that of the

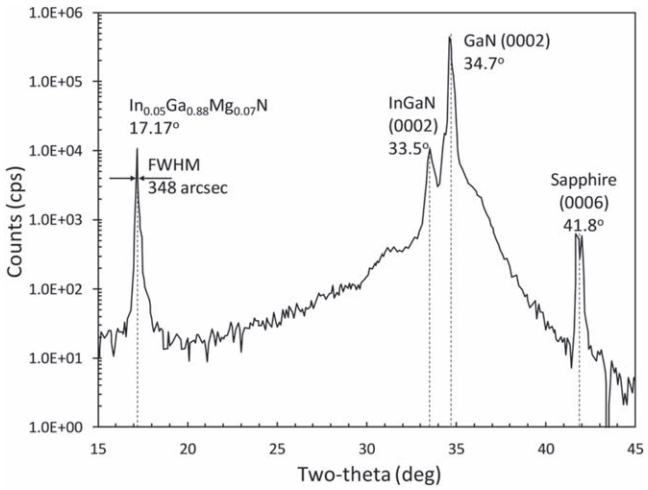

Figure 12. X-ray diffraction of the $In_{0.05}Ga_{0.88}Mg_{0.07}N$/InGaN/GaN/Sapphire film.

donors. Sample B2 has shown a net acceptor density of $\sim 4 \times 10^{18}\,cm^{-3}$ as illustrated in figure 11(a). In figure 11(b) the ECV measurement of an optimized InGaN:Mg film is presented. In this case the net acceptor concentration was found to range between $\sim 7 \times 10^{19}\,cm^{-3}$ and $\sim 2 \times 10^{19}\,cm^{-3}$. Sample B3 has been used for the fabrication of a mesa device. When forward biased electroluminescence is observed as seen in figure 11(c) demonstrating the formation of a good p–n junction structure. The strongest emission was measured at ~2.1 eV corresponding to photon emission from an InGaN alloy with an In fraction of ~35%. Conduction type and carrier concentration were measured using ECV. Sample B1 has shown an unstable conduction type which was dependent on the location of the measurement, suggesting that the density of the acceptors is roughly equal to that of the donors. Sample B2 has shown a net acceptor density of $\sim 4 \times 10^{18}\,cm^{-3}$ as illustrated in figure 11(a). In figure 11(b) the ECV measurement of an optimized InGaN:Mg film is presented. In this case the net acceptor concentration was found to range between $\sim 7 \times 10^{19}\,cm^{-3}$ and $\sim 2 \times 10^{19}\,cm^{-3}$. In figure 11(b) the ECV measurement of an optimized InGaN:Mg film is presented. In this case the net acceptor concentration was found to range between $\sim 7 \times 10^{19}\,cm^{-3}$ and $\sim 2 \times 10^{19}\,cm^{-3}$.

Sample B3 has been used for the fabrication of a mesa device. When forward biased electroluminescence is observed as seen in figure 11(c) demonstrating the formation of a good p–n junction structure. The strongest emission was measured at ~2.1 eV corresponding to photon emission from an InGaN alloy with an In fraction of ~35%.

3.6. (InGaMg)N alloy

(InGaMg)N quaternary alloy semiconductor films have not been synthesized and studied previously. There is one account of $Ga_{0.5}Mg_{0.5}N$ that was synthesized using a high-pressure, high-temperture method [35]. The GaMgN film was analyzed by x-ray diffraction (XRD) to determine the crystallinity and the lattice parameters, by energy dispersive x-ray to determine the composition and by absorption edge and photoluminescence (PL) to determine the energy gap of this material. The metal composition was found to be equally distributed between Ga and Mg each occupying 50% ± 3% of the respective lattice sites. The analysis of the structural data obtained from XRD has shown that the GaMgN has a hexagonal unit cell and the lattice parameters are a = 3.277 Å and c = 16.065 Å at room temperature. The band gap measured at 77 K was of ~3.1 eV.

We have investigated the samples A0–A4 through absorption, PL and XRD techniques and we have determined a band gap in the range from 2.55 to 2.8 eV. A detailed account of these measurements will be presented elsewhere. Figure 12 presents the x-ray diffraction of the sample A4 containing 7% Mg and ~5% In ($In_{0.05}Ga_{0.88}$ $Mg_{0.07}N$) that exhibits, besides the peaks corresponding to the sapphire substrate ($2\theta = 41.8°$), GaN ($2\theta = 34.7°$) and undoped InGaN ($2\theta = 33.5°$), a peak at $2\theta = 17.17°$, that we attribute to the InGaMgN alloy.

Using the position of the InGaN peak and considering the film unstrained we can estimate the film indium fraction to ~30%. The strong peak at $2\theta = 17.17°$ suggests that the atomic planes are parallel to the (0001) GaN planes while the low value of the full width at half maximum FWHM ≈ 348 arcsec suggest a good crystallinity. In a simplified way, assuming a negligible contribution from the strain and other sources of peak broadening, we can estimate the in-plane size of the crystallites using Scherrer relationship (4):

$$D = K\lambda/\beta \cos\theta. \quad (4)$$

Here D is the size of the coherent domain length, K is Scherrer constant, (usually assumed $K = 1$), λ is the wavelength of the radiation ($Cu_{(K\alpha)} = 1.5406$ Å), β is is the line broadening at half the maximum intensity (FWHM) in radians and $\theta = 8.58°$ is the Bragg angle. With these values we obtain a crystallite size of ~90 nm. The size of the lattice constant that defines the distance between the crystal planes (c) that are perpendicular on the diffraction vector can be determined using Bragg's formula (5):

$$n\lambda = 2c \sin(\theta). \quad (5)$$

For the (InGaMg)N peak position in the diffractogram of figure 12 we obtain a lattice constant c = 10.332 Å. The reduction in the c lattice constant from 16.065 Å for $Ga_{0.5}Mg_{0.5}$ N alloy appears as reasonable if the preponderance of Ga (88%) in lattice is considered.

4. Conclusions

InGaN films, doped with Mg, with high In content in the range from 30% to 40% were grown on GaN-on-sapphire templates by PA-MBE Mg doping was achieved using a wide range of Mg fluxes. We find that high Mg fluxes create high Mg surface densities able to disrupt the incorporation of In. The observed Mg incorporation behaviour in InGaN and the growth rate were found to be consistent with early accounts on the Mg flux effect on doping concentration and growth rate of GaN. When the Mg concentration at the surface is in the

range of up 10^{19} cm^{-3}, the impact on indium fraction is negligible [36]. For large Mg fluxes, the effect of Mg doping and the decrease of the fraction of In in InGaN has been described in the past [33]. However, under extreme Mg fluxes, In incorporation is, for the large part, prevented and the formation of a new quaternary (InGaMg)N alloy is observed. Based on the evidence at hand, these alloys form a new family of nitride semiconductors having a hexagonal lattice and an adjustable band gap extending across a portion of the solar spectrum, from 2.55 to 3.1 eV. XRD and TEM measurements demonstrate that this alloy has high crystallinity and a c-lattice constant of 10.332 Å. An explanation for the observed indium exclusion from the lattice is provided that rests on the thermodynamic tendency of Mg and Ga to replace In in the lattice. A flux modulation method is described that allows the growth of InGaN films that incorporate large fractions of Mg while maintaining In fractions as high as 40%. Using this method, successful p-type doping is demonstrated by the ECV measurement of net acceptor concentration as high as $\sim 7 \times 10^{19}$ cm^{-3} as well as the fabrication of light emission devices with an emission in the yellow-orange (596 nm) domain of visible spectrum. The range of group-III/Mg flux ratios (F_{III}/F_{Mg}) that allows doping without indium depletion was also determined.

Acknowledgments

This work was supported by RoseStreet Energy Laboratory, Contract LB07003462 and US DOD/DARPA under contract W91CRB-11-C-0012. We also acknowledge the financial support by City U SGP, Grant No. 9380076.

Data analysis and visualization was aided by SciDAVis application for Scientific Data Analysis and Visualization and by Daniel's XL Toolbox add-in for Excel.

ORCID iDs

Iulian Gherasoiu https://orcid.org/0000-0003-4206-5534

References

[1] Wu J, Walukiewicz W, Yu K M, Ager J W III, Haller E E, Lu H and Schaff W J 2003 Narrow bandgap group III-nitride alloys *Phys. Status Solidi* b **240** 412–6

[2] Hsu L and Walukiewicz W 2008 Modeling of InGaN/Si tandem solar cells *J. Appl. Phys.* **104** 024507

[3] Zhang X, Wang X, Xiao H, Yang C, Ran J, Wang C, Hou Q, Li J and Wang Z 2008 Theoretical design and performance of $In_x Ga_{1-x} N$ two-junction solar cells *J. Phys. D: Appl. Phys.* **41** 245104

[4] Siyu L and Xiaosheng Q 2011 AlGaAs/GaAs tunnel junctions in a 4-J tandem solar cell *J. Semicond.* **32** 112003

[5] Chee K W A and Hu Y 2018 Design and optimization of ARC less InGaP/GaAs single-/multi-junction solar cells with tunnel junction and back surface field layers *Superlattices Microstruct.* **119** 25–39

[6] Neamen D A 2012 *Semiconductor Physics and Devices-Basic Principles* 4th Edn. (New York: McGraw-Hill)

[7] Ajay A, Schörmann J, Jiménez-Rodriguez M, Lim1 C B, Walther F, Rohnke M, Mouton I, Amichi L, Bougerol C and Den Hertog M I 2016 Ge doping of GaN beyond the Mott transition *J. Phys. D: Appl. Phys.* **49** 445301

[8] Gherasoiu I, Yu K M, Reichertz L A and Walukiewicz W 2014 InGaN doping for high carrier concentration in plasma-assisted molecular beam epitaxy *Phys. Status Solidi.* c **11** 381–4

[9] Fiorentini V, Bernardini F, Bosin A and Vanderbilt D 1996 *Ab initio* shallow acceptor levels in gallium nitride *The Physics of Semiconductors* (Singapore: World Scientific)

[10] Huang J W, Kuech T F, Lu H and Bhat I 1996 Electrical characterization of Mg-doped GaN grown by metalorganic vapor phase epitaxy *Appl. Phys. Lett.* **68** 17

[11] Gotz W, Kern R S, Chen C H, Liu H, Steigerwald D A and Fletcher R M 1999 Hall-effect characterization of III–V nitride semiconductors for high efficiency light emitting diodes *Mater. Sci. Eng.* B **59**

[12] Kumakura K, Makimoto T and Kobayashi N 2003 Mg-acceptor activation mechanism and transport characteristics in p-type InGaN grown by metalorganic vapor phase epitaxy *J. Appl. Phys.* **93** 3370

[13] Pantha B N, Sedhain A, Li J, Lin J Y and Jianga H X 2009 Electrical and optical properties of p-type InGaN *Appl. Phys. Lett.* **95** 261904

[14] Zhao C-Z, Wei T, Chen L-Y, Wang S-S and Wang J 2017 The activation energy for Mg acceptor in the Ga-rich InGaN alloys *Superlattices Microstruct.* **102** 40–4

[15] Li S X, Yu K M, Wu J, Jones R E, Walukiewicz W, Ager J W III, Shan W, Haller E E, Lu H and Schaff W J 2005 Fermi-level stabilization energy in group III nitrides *Phys. Rev.* B **71** 161201

[16] Gherasoiu I, O'Steen M, Bird T, Gotthold D, Chandolu A, Song D Y, Xu S X, Holtz M, Nikishin S A and Schaff W J 2008 Growth of high quality InN on production style PA-MBE system *Phys. Status. Solidi.* c **5** 1642–4

[17] Namkoong G, Trybus E, Lee K K, Moseley M, Doolittle W A and Look D C 2008 Metal modulation epitaxy growth for extremely high hole concentrations above 10^{19} cm^{-3} in GaN *Appl. Phys. Lett.* **93** 172112

[18] Heying B, Averbeck R, Chen L F, Haus E, Riechert H and Speck J S 2000 Control of GaN surface morphologies using plasma-assisted molecular beam epitaxy *J. Appl. Phys.* **88** 10.1063

[19] Chen H, Feenstra R M, Northrup J E, Zywietz T, Neugebauer J and Greve D W 2000 Surface structures and growth kinetics of InGaN(0001) grown by molecular beam epitaxy *J. Vac. Sci. Technol.* B **18** 2284

[20] Moustakas T D and Bhattacharyya A 2011 Experimental evidence that the plasma-assisted MBE growth of nitride alloys is a liquid phase epitaxy process *ECS Trans.* **35** 63–71

[21] Guha S, Bojarczuk N A and Cardone F 1997 Mg in GaN: Incorporation of a volatile species at high temperatures during molecular beam epitaxy *Appl. Phys. Lett.* **71** 1685

[22] Orton J W, Foxon C T, Cheng T S, Hooper S E, Novikov S V, Ber B Y and Kudriavtsev Y A 1999 Incorporation of Mg in GaN grown by molecular beam epitaxy *J. Cryst. Growth* **197** 7–11

[23] Bungaro C, Rapcewicz K and Bernholc J 1999 Surface sensitivity of impurity incorporation: Mg at GaN (0001) surfaces *Pys. Rev.* B **59** 9771–4

[24] Daudin B, Mula G and Peyla P 2000 Mg-modified surface kinetics of the GaN growth by molecular beam epitaxy *Phys. Rev.* B **61** 10330–5

[25] Valdueza-Felip S, Bellet-Amalric E, Nunez-Cascajero A, Wang Y, Chauvat M-P, Ruterana P, Pouget S, Lorenz K, Alves E and Monroy E 2014 High In-content InGaN layers synthesized by plasma-assisted molecular-beam epitaxy:

growth conditions, strain relaxation, and In incorporation kinetics *J. Appl. Phys.* **116** 233504

[26] Karpov S Y 1998 Suppression of phase separation in InGaN due to elastic strain *MRS Internet J. Nitride Semicond. Res.* **3** 16

[27] Doppalapudia D, Basu S N, Ludwig K F Jr and Moustakas T D 1998 Phase separation and ordering in InGaN alloys grown by molecular beam epitaxy *J. Appl. Phys.* **84** 1389–95

[28] Duff A I, Lymperakis L and Neugebauer J 2014 Understanding and controlling indium incorporation and surface segregation on $In_xGa_{1-x}N$ surfaces: an *ab initio* approach *Phys. Rev.* B **89** 085307

[29] Belabbes A, Furthmuller J and Bechstedt F 2013 *Ab-initio* study of Mg-doped InN(0001) surface *AIP Adv.* **3** 012102

[30] Devore J L 2012 *Probability and Statistics for Engineering and the Sciences* 8th Edn. (Boston: Brooks/Cole)

[31] Wood C E C, Desimone D, Singer K and Wicks G W 1982 Magnesium- and calcium-doping behavior in molecular-beam epitaxial III–V compounds *J. Appl. Phys.* **53** 4230

[32] Liliental-Weber Z, Benamara M, Washburn J, Domagala J Z, Piner E L, Roberts J C and Bedair S M 2001 Relaxation of InGaN thin layers observed by x-ray and transmission electron microscopy studies *J. Elec. Mater.* **30** 439

[33] Hawkridge M E, Liliental-Weber Z, Yu K M, Reichertz L A, Schaff W J, Ager J W and Walukiewicz W 2009 Stacking faults and phase changes in Mg-doped InGaN grown on Si *Phys. Status Solidi* c **6** S421–4

[34] Li Q 2018 *Strain Relaxation in InGaN/GaN herostructures* Normandie Université https://tel.archives-ouvertes.fr/tel-01775272/document

[35] Suski T, Perlin P, Pietraszko A, Leszczynski M, Bockowski M, Grzegory I and Porowski S 1999 GaMg)N–New Wide Band Gap Semiconductor *Phys. Status Solidi* a **176** 343

[36] Valdueza-Felip S, Ajay A, Redaelli L, Chauvat M P, Ruterana P, Cremel T, Jiménez-Rodríguez M, Kheng K and Monroy E 2017 P-i-n InGaN homojunctions (10%–40% In) synthesized by plasma-assisted molecular beam epitaxy with extended photoresponse to 600 nm *Sol. Energy Mater. Sol. Cells* **160** 355–60